NTNU – Trondheim
Norwegian University of
Science and Technology

Magnetic Resonance Imaging: Multidimensional non-Gaussian Diffusion-weighted MRI

Image quality analysis

Jens Wergeland Meisingset

Master of Science in Physics and Mathematics
Submission date: June 2015
Supervisor: Pål Erik Goa, IFY

Norwegian University of Science and Technology
Department of Physics

Preface

This thesis describes the work undertaken within the subject TFY4900 - Physics, Master's Thesis spring 2015 at the Norwegian University of Science and Technology (NTNU). The work is carried out in cooperation with St. Olavs Hospital. The goal for this project is to compare the image quality on two different 3T scanners, with two different diffusion gradient setups, to ascertain which combination of these provides the best foundation for highly diffusion weighted, multidimensional nuclear magnetic resonance imaging analysis.

Trondheim, June 18, 2015
Jens Wergeland Meisingset

Abstract

To investigate the viability of two different nuclear magnetic resonance imaging systems for acquisition of highly diffusion weighted, multidimensional human brain data, images were acquired on both, using two different diffusion sensitizing gradient setups. The sequence used was a diffusion weighted spin echo sequence with an echo planar read out. The diffusion gradients tested were monopolar and twice-refocused bipolar. These were used to acquire data on a Siemens Prisma and Skyra scanner. The data acquired with monopolar gradients on the Prisma scanner suffered from eddy current induced geometric distortions, while the bipolar scan on the Prisma and both Skyra acquisitions displayed lower signal to noise ratios. The difference between bipolar and monopolar signal intensity was noticeably greater on the Prisma system, due to an unexpectedly large drop when utilizing bipolar gradients. Background noise level were lower overall on the Prisma system, but particularly on the images acquired without diffusion weighting, due to the Skyra system experiencing a significant increase in background noise levels when not using diffusion gradients. Eddy current correction was unsuccessful for the Prisma monopolar sequence when using affine transformation with 12 degrees of freedom. Removal of non-brain matter proved difficult, due to the software having problems differentiating between background noise and brain matter in images with low signal to noise ratio. Of the scanner and gradient setup combinations tested, the Prisma scanner, using a bipolar gradient setup appears to be the superior choice, despite having comparable signal to noise ratio with the Skyra systems.

Sammendrag

For å undersøke anvendbarheten til to forskjellige nukleær magnetisk resonans avbildningssystemer for å anskaffelse av diffusjonvektet, multidirektional menneskehjernedata Bilder ble samlet inn på begge, med to forskjellige diffusjon-vektende gradientoppsett. Sekvensen som ble anvendt var en diffusjons-veid spinnekkosekvens med et ekkoplanar utlesning. Gradientene som ble testet var monopolar og dobbelt-refokuserte bipolar. Disse ble brukt til å samle inn data på en Siemens- Prisma og Skyra skanner. Dataene med monopolare gradienter på Prisma systemet led av geometriske forvrengninger indusert av uønskede strømmer, imens den bipolare scannen på Prisma og begge Skyra scannene hadde svakere signal-støyforhold. Forskjellen mellom bipolare og monopolare signalintensiteter var merkbart større i Prisma systemet, på grunn av en uventet stor tap ved benyttelse av bipolare gradienter. Bakgrunnsstøynivået var lavere på Prisma systemet, men spesielt på bildene ervervet uten diffusjonvekting, på grunn av Skyra systemet opplevede en betydelig økning i bakgrunnsstøy i bilder uten diffusjonvekting. Korreksjon av geometriske fordreiningen som følge av induserte strømmer var mislykket for Prisma bildene med monopolar diffusjonsvekting ved bruk av "affine" transformasjonen med tolv frihetsgrader. Fjerning av ikke-hjernemasse viste seg å være vanskelig, på grunn av at programvaren hadde problemer med å skille mellom bakgrunnsstøy og hjernemasse i bilder med lavt signal-støyforhold. Av de skanner- og gradient kombinasjonene som er blitt testet, fremstår Prisma skanneren med bipolart gradientoppsett som det beste valget, til tross for et sammenlignbart signal-støyforhold med Skyra systemet.

Acknowledgements

The work done in this thesis would not have been started without Anders Kristoffersen, who served as the main motivator for the project. He provided valuable insights and also served to kindle my own interest in the project. I would also like to offer my thanks to the staff at the Haukeland hospital in Bergen, who were very forthcoming and helpful during our experiment on their Siemens Prisma system. My supervisor, Pål Erik Goa has been an invaluable companion during the entire project, giving advice and encouragement equal measures. Even without his pristine academic guidance, for me, simply being regularly reminded that the path of a scientist is supposed to be a really winding one, has been very important. Last but not least, I would like to thank my fiance. Without her, I would not have made it all the way to the end without succumbing to the pressure and workload. Thank you all for enabling me in this.

Jens W. Meisingset

Trondheim, June 18, 2015

Abbreviations

ADC	Apparent diffusion constant
EPI	Echo planar imaging
DKI	Diffusion kurtosis imaging
DTI	Diffusion tensor imaging
DW	Diffusion-weighted
FID	Free induction decay
NMR	Nuclear magnetic resonance
NMRI	Nuclear magnetic resonance imaging
PE	Phase encoding (gradient)
RF	Radio frequency
RO	Read out (gradient)
ROI	Region of interest
SE	Spin echo
SEDW	Spin echo diffusion-weighing
SNR	Signal to noise ratio
SS	Slice selection

Contents

Preface i
Abstract iii
Sammendrag v
Acknowledegements vii
Abbreviations ix

1 Introduction **1**

2 Theory **3**
2.1 Introduction to the Nuclear Magnetic Resonance Phenomenon 3
2.1.1 Introductory Nuclear Magnetic Resonance 3
2.2 Nuclear Magnetic Resonance Imaging 7
2.2.1 Image Noise and Signal 7
2.2.2 Spin Echo Sequence 8
2.2.3 Echo Planar 10
2.2.4 k-Space Trajectory 10
2.2.5 Diffusion-Weighting 12
2.3 Eddy Current 14
2.4 Affine Transformation 15

3 Method **17**
3.1 Data Post-Processing 20

4 Result **21**
4.1 Raw Data 21
4.2 Measurements 24
4.3 Eddy Current Analysis 31

5 Discussion **35**

6 Conclusion **39**
6.1 Future Work 39

A Sequence parameters **43**

1 Introduction

Diffusion-Weighted Magnetic Resonance Imaging is a non-invasive medical imaging modality which provides image contrast according the imaged objects diffusivity in addition to the other intrinsic properties of the object, such as proton density, T_1 and T_2*. By considering the difference in signal loss in experiments with different diffusion-weighting (DW) factors, usually denoted b, an apparent diffusion coefficient (ADC) may be calculated for each voxel. The ADC in this case, is only measured for a single direction and does not differentiate between diffusion, i.e. Brownian motion, and other sources of intravoxel random movement.

In diffusion tensor imaging (DTI), a minimum of six directions are used where b-values around 1000 s/mm^2 are standard. DTI data can be used to calculate a plethora of useful metrics, e.g. ADC-maps, fractional anisotropy and TRACE images. The increase in b-value, also allows for a finer tissue separation based on variations in the diffusion present, while the use of multiple directions provides the opportunity to separate tissue based on the anisotropy of the diffusion. The signal equation used in DTI assumes unrestricted diffusion, which entails that the signal decay will have a Gaussian form. This is not what is seen experimentally for increased DW. Due to tissue microstructurs and similar boundaries that limit diffusion, the signal loss due to the DW begins to level off for values of b exceeding ≈ 1000 s/mm^2. Diffusion kurtosis imaging (DKI) includes a metric for the kurtosis of the signal decay, to quantify its deviation from a Gaussian distribution.

Proper analysis of either DTI or DKI data necessitates a certain level of image quality. The common metrics used to define image quality are signal strength and noise level in the image, often together as signal to noise ratio (SNR). For DKI data, where DW values ranging from $b = 0$ to 5000 s/mm^2 are not uncommon, the SNR needs to be large enough to provide sufficient contrast for the images with large b-values. The noise is unaffected by the increase in b, but the signal strength is reduced.

Another important aspect, common for both DTI and DKI analysis, is that image comparisons for different directions or DW are done on a voxel-to-voxel basis. Therefore, it is important that each pixel in the image always display the same part of the object. If

this is not the case, it can be the result of actual object motion or a variety of image artifacts that distorts the image, e.g. susceptibility, fat-water shift, Nyquist-ghosting and eddy currents. Similarly, since the data analysis is intensity-based, artifacts that affect image intensity, e.g. Gibs phenomenon and Nyquist-ghosing, must also be corrected for if present.

The main motivator for this thesis is to continue the work from Kristoffersen [1], to use Pade-approximants to model the signal decay in DKI data. Two requirements must be met for such an analysis. The model used in this article would need to be converted into a tensor format, and data sets of sufficient quality. To this end, a DKI sequence was designed and used to acquire data on two different 3T scanners, with two different diffusion gradient setups.

This thesis will provide a rudimentary introduction to nuclear magnetic resonance (NMR) physics, before introducing the relevant imaging terminology in the following section.

The goal of this thesis is to ascertain whether the images, whose acquisition is outlined in the methods chapter, are of sufficient quality to be utilized for their intended purpose.

2 Theory

This chapter aims to provide a basic introduction to the phenomenon that is nuclear magnetic resonance and the utilization of this as a medical imaging modality. After an initial description to the underlying physics, applications of this relevant to the thesis will be introduced

2.1 Introduction to the Nuclear Magnetic Resonance Phenomenon

Nuclear magnetic resonance is a quantum mechanical phenomenon that can be adequately described using classical physics. While only quantum mechanics provides a complete explanation for the phenomenon, it fails to provide intuitive understanding and thus the classical description see more usage due to its visual and relatable nature.

For this thesis, a classical description will be sufficient to cover the relevant theory, but for those interested, an in-depth account of the underlying quantum mechanical concepts can be found in [2].

2.1.1 Introductory Nuclear Magnetic Resonance

A fundamental principle in NMR is that when exposed to an external magnetic field, the magnetic moment, μ, of protons will precess at a frequency proportional to the magnetic field strength:

$$\omega_0 = \frac{\gamma}{2\pi} B_0. \tag{2.1}$$

This equation is commonly referred to as the Larmor equation, and gives us the value of the Larmor frequency, ω_0. Here B_0 is the magnetic field strength and γ is the gyromagnetic ratio, equal to 42.58 MHz/T for protons [2].

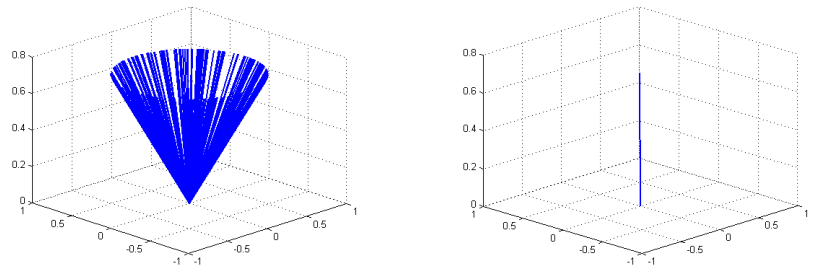

(a) ***(b)***

Figure 2.1: *Visualization of the magnetic momenta cancellation in all directions but the magnetic field axis. (a) Magnetic momenta precessing in a static magnetic field, oriented parallel to the vertical axis. (b) The summations of all the vectors results in only the vertical component remaining.*

The contributions of all the precessing protons cancel each other out in all but the direction of the magnetic field, resulting in a magnetization vector, M_z, parallel to the static magnetic field. This is shown in Figure 2.1.

To utilize this magnetization for NMR imaging (NMRI), it needs to have a component perpendicular to the static magnetic field. Therefore a magnetic field, B_1, rotating at a frequency close to the proton resonance frequency, i.e. Larmor frequency, is temporarily introduced to flip the magnetization vector down into the transverse plane. This magnetic field is interchangeably referred to as an radio frequency (RF) pulse.

Initially, the magnetization vector, $\vec{M}$, does not precess around the axis of the static magnetic field, B_0, but it will do so after excitation by the RF pulse. In terms of a coordinate system, if the original magnetization vector was along the z-axis, the excited magnetization will be flipped down into the xy-plane, denoted M_{xy}, rotating around the origin, i.e. around the z-axis. It is customary to simplify this by visualizing the magnetization in a rotating coordinate system, where z is stationary, and x' and y' are rotating around origin at the Larmor frequency from equation (2.1), resulting in a stationary transverse magnetization.

The magnetization vector stems from Felix Bloch's original paper on nuclear induction [3]. He formulated what is now known as the Bloch-equations, which describe the evolution of the magnetization vector components over time. Using the Bloch-equations (for the derivation, the reader is referred to [2] and [3]), the subsequent change in magnetization over time after being excited, i.e. M_0 realigning with B_0, can be expressed by the following equations:

$$M_{\parallel}(t) = M_0(1 - e^{-t/T_1}) \tag{2.2}$$

$$M_{\perp}(t) = M_0 e^{-t/T_2} \tag{2.3}$$

$M_{\parallel}$, or $M_z(t=0)$, is the initial magnetization along the z-axis due to the static magnetic field and T_1 is the longitudinal relaxation time constant. $M_{\perp}$, or $M_{x'y'}$, is the magnitude of the magnetization in the xy-plane and T_2 is the relaxation time constant for the transverse magnetization decay.

Physically, T_1 is regrowth of the longitudinal magnetization, $M_{\parallel}$, due to energy being released. It is sometimes referred to as 'thermal relaxation' or 'spin-lattice relaxation'[1]. T_2 is the loss of phase coherence, due to inhomogeneities in the static magnetic field or local variations in precessional frequencies. Usually T_2 is denoted T_2^*, which is the reciprocal sum of the static and dynamic dephasing decay constants:

$$\frac{1}{T_2^*} = \frac{1}{T_2'} + \frac{1}{T_2} \tag{2.4}$$

Here T_2' is the static dephasing, and T_2 is the dynamic dephasing. As will be discussed further in Section 2.2.2, the static dephasing is reversible, which is the crux of the spin echo (SE) imaging method.

Spatial encoding is achieved by using gradients. In NMRI a gradient is a concomitant magnetic field, parallel to the static magnetic field, whose strength varies linearly as a function of position. By introducing a gradient, G, in an arbitrary direction, for instance along the x-axis, equation (2.1), becomes

$$\omega(x) = \frac{\gamma}{2\pi}(B_0 + G_x x). \tag{2.5}$$

The precessional angular frequency, $\omega(x)$, is then linearly dependent on x. This can be seen in Figure 2.2. In NMRI this is done for the z, y and x axis, and their gradients are called G_{SS}; slice selection (SS), G_{PE}; phase encoding (PE), and G_{RO}; read out (RO).

The signal from for a sample exposed to two gradients can be expressed by the following equation

$$S(x,y) \propto \iint_{object} M_{\perp}(x,y) e^{-i2\pi(k_x x + k_y y)} dk_x dk_y \tag{2.6}$$

where S is the signal and k, the wave number, is defined as follows

$$k_i(t) \equiv \frac{\gamma}{2\pi} \int_0^t G_i(\tau) d\tau. \tag{2.7}$$

[1]Historically, due to MR having it's origin in examining crystalline structures

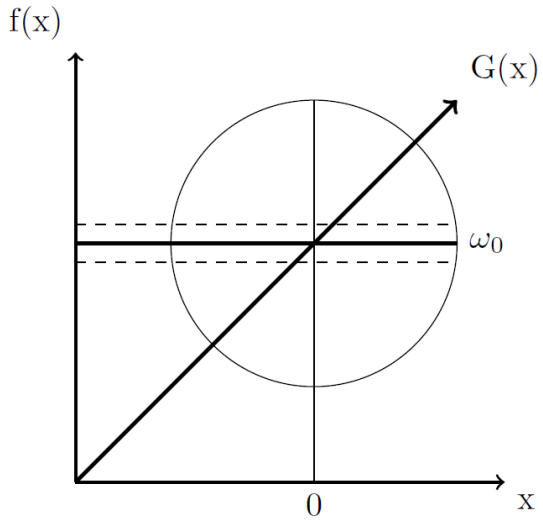

Figure 2.2: *Spatial encoding for a single dimension. Due to the addition of a gradient $G(x)$, the precessional frequency varies spatially as a function of x. Dashed lines indicate bandwidth, i.e. range of frequencies.*

Here G_i is the gradient G_x,G_y or G_z. It is because of this substitution that Fourier space is commonly referred to as k-Space in NMRI literature.

2.2 Nuclear Magnetic Resonance Imaging

For this thesis, data acquisition was primarily done using a spin echo diffusion-weighted (SEDW) sequence with an Echo-Planar RO. The specific sequence parameters can be found in Chapter 3. The following subsections will aim to shed some light on the NMRI sequence terminology used.

2.2.1 Image Noise and Signal

NMRI acquisitions will be contaminated by white noise. Sources of this include the object being imaged and the electric circuitry in receiver chain. Available signal depends on the object, e.g. spin density, T_1, T_2, and hardware factors such as B_0 and available gradient system. In addition to these, there are several sequence parameters that affect the final SNR of the image, e.g. bandwidth, *TR*, *TE*, number of averages acquired and voxel size.

The acquired complex signal in NMRI will initially have a Gaussian distribution. This is also true for the real and imaginary images that results from using a complex Fourier transform on the signal, due to the linear and orthogonal nature of the Fourier transform [4]. A common form to present NMRI data is by using magnitude reconstructed images. These are created by taking the magnitude of the acquired imaginary and real images, thus discarding any phase information but also avoiding complications due to phase-related artefacts.

$$S_{\text{pixel}} = \sqrt{R^2 + I^2}$$

Here S_{pixel} denotes pixel intensity, while R and I are the corresponding pixel in the real and imaginary images, respectively. The resulting magnitude image will have a Rician signal distribution [5],

$$P_M(M) = \frac{M}{\sigma^2} e^{-\frac{M^2+A^2}{2\sigma^2}} I_0\left(\frac{A \cdot M}{\sigma^2}\right), \tag{2.8}$$

where M and A are the measured and true signal intensities for each pixel, I_0 is the modified zeroth order Bessel function and σ is the standard deviation from the Gaussian distribution of the original real and imaginary images.

For areas in the magnitude image where no signal is present, the noise will have a Rayleigh probability distribution, which is a special case of the Rice distribution.

$$P_M(M) = \frac{M}{\sigma^2} e^{-\frac{M^2}{2\sigma^2}} \tag{2.9}$$

For the Rayleigh distribution, the mean and variance is defined as

$$\mu = \sqrt{\frac{\pi}{2}}\sigma \tag{2.10}$$

and

$$VAR = \frac{4-\pi}{2}\sigma^2. \tag{2.11}$$

2.2.2 Spin Echo Sequence

Spin Echo is a sequence setup that applies a secondary RF pulse at a time $TE/2$ after the initial RF pulse [6]. The first pulse flips the magnetization vector $\vec{M}$ down into the xy-plane. The individual magnetic momenta will then start to dephase according to the object's T_2^*, i.e. T_2' and T_2 values (see Section 2.1). The second RF pulse, commonly referred to as the 180° pulse, flips the spins around, still in the xy-plane, at a time $TE/2$. The spins will then rephase, creating a signal 'echo' at time TE, whose peak intensity will only depend on the dynamic dephasing, or T_2. The dephasing caused by T_2' due to spatial field variations is cancelled out by this flipping, which reverses the static dephasing. A standard SE sequence is shown in Figure 2.3. The signal equation for the SE is as follows

$$S = M_0(1 - 2e^{-\frac{TR-\frac{TE}{2}}{T_1}} + e^{-\frac{TR}{T_1}})e^{-\frac{TE}{T_2}}$$

Here S is the signal intensity, TR is the repetition time and TE is the echo time. For $TR \gg TE/2$, the equation can be simplified.

$$S = M_0(1 - e^{-\frac{TR}{T_1}})e^{-\frac{TE}{T_2}} \tag{2.12}$$

which is the signal equation for SE sequences where the assumption $TR >> TE/2$ holds. Another important assumption made, is that $TR >> T_2$, so that no lingering in-plane magnetization is refocused by the RF pulse.

Figure 2.3 shows a simplified SE setup. $M_\perp$ is the actual measurable signal, which initially has a magnitude of M_0. After the first 90° RF pulse at $t = 0$, the transverse magnetization suffers a signal loss according to the T_2^* relaxation time constant. At t=$TE/2$ the static dephasing is reversed by the 180° RF pulse, and as a result an 'echo' appears at time t=TE, which will have a signal intensity according to equation (2.12). $M_\parallel$ experiences a regrowth in accordance with T_1. Note that while the gradient pulses are drawn as rectangles, they are actually trapezoid, with finite ramp times.

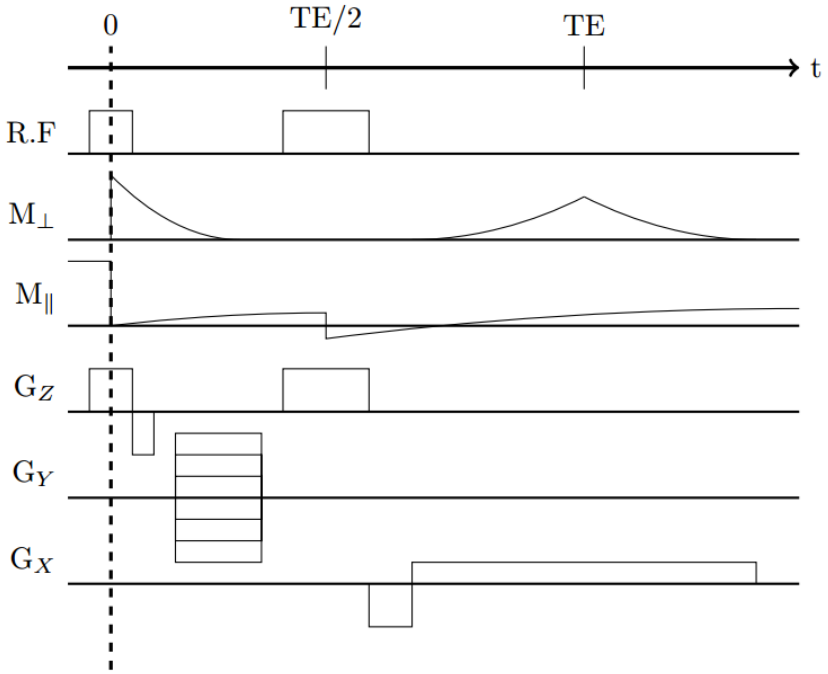

Figure 2.3: *Standard SE gradient setup $M_\perp$ and $M_\parallel$ are the transverse and longitudinal magnetization, G_Z,G_Y and G_X are the encoding gradients for each spatial dimension, often denoted SS, PE and RO, respectively.*

G_Z is turned on during the RF pulses to ensure that the correct slices are excited. The following negative gradient lobe is necessary because the G_Z pulse applied during the 90° causes a dephasing along the z-axis. The same is true for 180°, but because of the reversing property of this pulse, no negative gradient lobe is necessary. For each G_Y, the entire sequence is repeated after a time TR. Thus, the total imaging time equals the number of chosen values for G_Y multiplied by TR.

G_X, or the RO gradient, dephases the spins, then rephases them. During this rephasing, i.e. positive gradient, the signal is measured. The dephasing lobe will in practice also be positive, and placed on the opposite side of the 180° RF pulse, which is equivalent to having them of opposite polarity, but on the same side of the second RF pulse. While equivalent, the former option will ensure less hardware strain. The latter gradient juxtaposition was chosen here to highlight their connection, but the former is nonetheless shown in Figure 2.4.

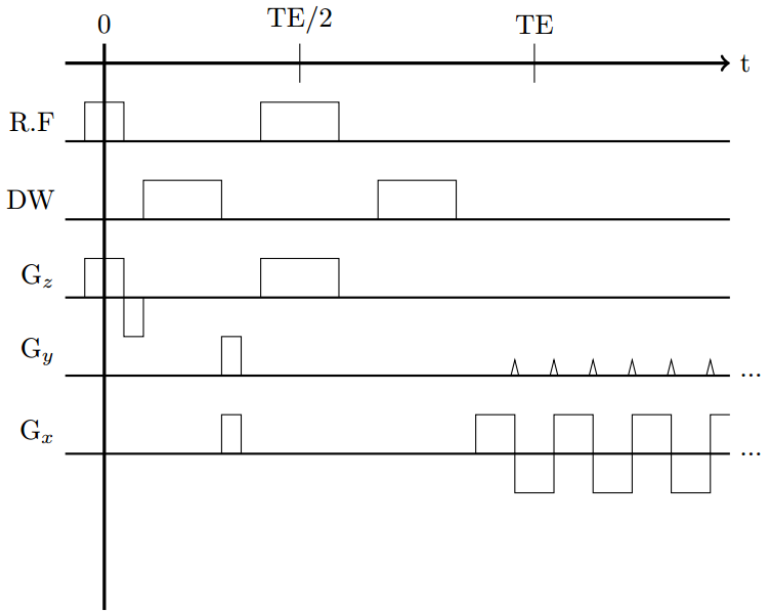

Figure 2.4: *Standard DW Echo-Planar Imaging gradient setup. The RF pulses and G_z are unchanged from Figure 2.3. G_y and G_x are equal in function from Figure 2.3, but an entire image is collected during a single echo. For DW a pair of diffusion sensitizing gradient pulses have been added.*

2.2.3 Echo Planar

Echo planar imaging, or EPI, is a very fast imaging technique. The reduction in scanning time stems from utilizing only one RF pulse excitation of the sample to acquire the entire image [7]. This is possible due to the "train" of G_x pulses continuously dephasing and rephasing the sample, while interspersed G_y phase-encoding blips slowly increment the phase along k_y-axis. By only requiring a single RF excitation induced echo, imaging time is greatly reduced. A peculiarity in EPI is the difference between bandwidth for the frequency and phase encoded directions. In NMRI, bandwidth is measured as Hz/pixel, which describes the stepwise frequency increase between adjacent pixels. Since an entire image row is acquired for a single step along the phase encoded direction, the bandwidth in the frequency direction will be larger by a factor equal to the resolution in this direction. This discrepancy is illustrated in Figure 2.5.

2.2.4 k-Space Trajectory

Figure 2.5 shows movement though k-space in a blipped EPI-sequence like the one shown in Figure 2.3. The RO and PE gradients are initially turned on preceding the actual

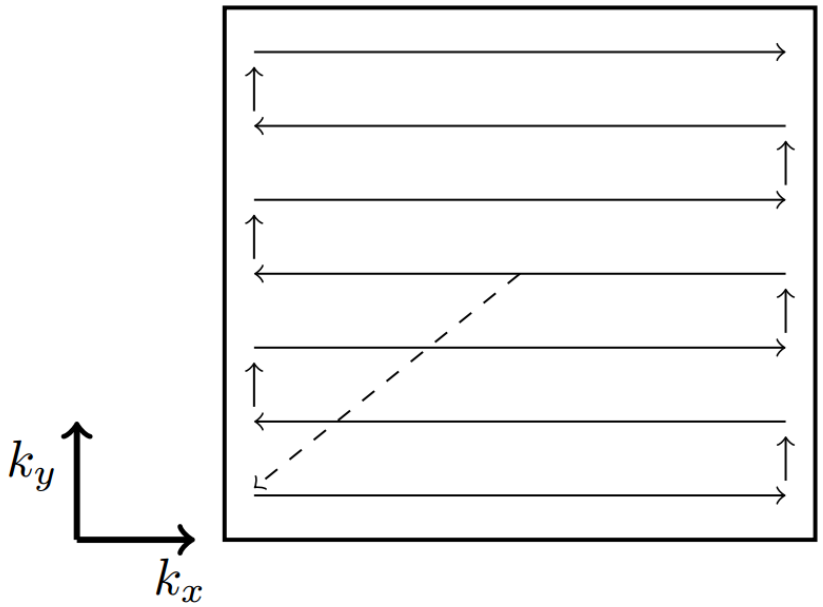

Figure 2.5: *Visualization of k-space measurement during a standard EPI sequence. k_x and k_y are related to the RO and the PE gradient, respectively. The dashed lines indicate movement preceding the actual measurement due to the dephasing lobes.*

signal acquisition. This is commonly referred to as a dephasing lobe. The purpose of this is to adjust the starting position in k-space before the measurement, so that an entire row in k-space can be covered during the signal RO. Each pulse by the RO gradient covers a line in k-Space, and each PE gradient blip adjusts the position so that a new line can be read. Since the RO gradient pulses are alternating between positive and negative values, the same also applies to the the read-direction for adjacent lines in k-Space. This method of k-Space traversal, the zig-zag pattern, has the benefit of providing raw data in the form of points on an equidistant grid. The equidistance is a necessary criteria that must be fulfilled before a Fourier transform can be applied. A frequently utilized attribute of k-space is its inherent symmetry, which can be exploited to reduce acquisition times.

Partial Fourier is based on the symmetric nature of k-space around the center, or $k = 0$, i.e. that the real signal component is symmetric with respect to the origin, while the imaginary component is anti-symmetric. Knowing this, and possessing measured data from at least half of k-space, the rest can be calculated during the reconstruction. In practice the conjugate symmetry assumption is not necessarily accurate, due to phase variations caused by e.g. field inhomogeneities, object motion.

2.2.5 Diffusion-Weighting

Diffusion-weighted SE imaging uses gradients to reduce the signal from moving spins. This is done by applying two diffusion sensitizing gradient pulses of equal length and magnitude on either side of the 180° RF pulse. The magnitude of these pulses is denoted b, and is measured in s/mm^2.

For stationary spins, these pulses will first dephase, then rephase the spins again immediately following the 180° RF pulse. This is, however, only true for stationary spins. Diffusing spins will not be completely rephased by the second gradient pulse, and will therefore have a reduced signal intensity in the image. The DW sequence will generally be repeated a number of times, first without the diffusion gradient pulses, then a number of times with incrementally increasing diffusion gradient strengths. The loss of intensity will be correlated to the speed at which spins diffuse in the object. [8] [9]

The pulse setup shown in Figure 2.4 is also shown in Figure 2.6. The bipolar setup has two sets of dephasing and rephasing pulses, placed on either side of the 180° RF pulse, making each side equal to the unipolar setup. While this causes an increase in the minimum possible TE for the sequence, it provides other benefits, e.g. reduced effect of first-order Eddy current distortions. [10]

Diffusion Signal

In DW imaging, the magnitude of the DW is defined in terms of the parameter b. For rectangular pulses, monopolar pulses, this is defined as

$$b = \gamma^2 A^2 \delta^2 \left(\Delta - \frac{\delta}{3} \right), \tag{2.13}$$

where the parameters are shown in Figure 2.6 [9]. For free, unrestricted diffusion, where spins are only affected by brownian motion, the probability of the particle remaining inside the imaging volume after an arbitrary duration, has a gaussian distribution. Assuming free diffusion, the following expression for the signal as a function of b emerges

$$S(b) \approx S_0 e^{-bD}. \tag{2.14}$$

Here S_0 is the signal intensity in the absence of any form of DW and D is called the ADC for *in vivo* diffusion measurements, since the registered signal loss might be due to additional contributions from other factors, e.g. flow. This equation is commonly used when fitting acquired DTI data to find the ADC, but for increased values of b it provides a poorer fit. This is because the assumption of free diffusion does not hold for higher values of b, since biological tissue contains microstructures that inhibit diffusion. For values of $b > 1000$ s/mm^2, the signal loss levels off whereas the free diffusion model predicts a continued decay.

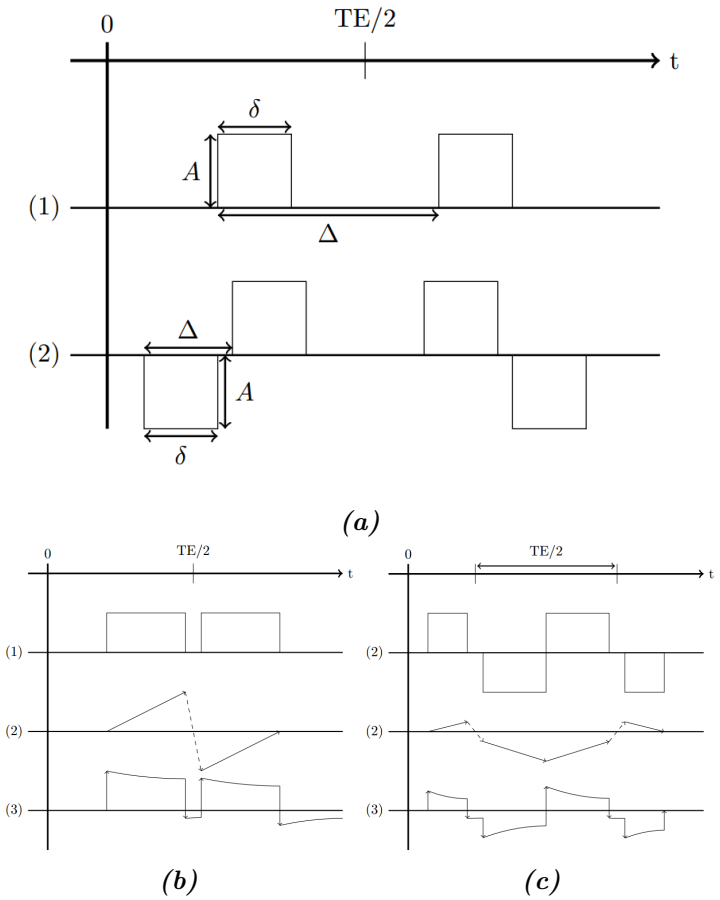

Figure 2.6: *Illustration of the diffusion gradient setups utilized. (a) shows the principal difference between the monopolar (1) and bipolar (2) gradient setups, and also defines the parameters that are used to calculate DW, b. A is the pulse amplitude, δ is the pulse duration while Δ is the elapsed time from a dephasing to the subsequent rephasing. (b-c) are the Monopolar and Bipolar setups, respectively, with (2) the phase evolution for stationary spins and (3) eddy current accumulation.*

For sequences utilizing higher values of b it is therefore necessary to include additional terms to account for deviations from the Gaussian distribution.

$$\begin{aligned} \ln S(b) &= \sum_{i=0}^{\infty} C_i b^i \\ &= C_0 + C_1 b + C_2 b^2 + ... \end{aligned} \tag{2.15}$$

For DKI, an additional term from equation (2.15) is usually added, resulting in the following equation.

$$S(b) \approx S_0 e^{-bD+C_2 b^2} \tag{2.16}$$

Here, the addition of the term C_2 allows for a better curve fit for the data. It also quantifies the data's deviation from a Gaussian distribution, or the data's non-gaussanity.

2.3 Eddy Current

Eddy currents are unwanted electrical currents that are induced in the gradient coils by the gradients' magnetic fields. By altering the spatial encoding provided by the static magnetic field in conjunction with the applied gradients, geometric distortions occur. The nature of these distortions becomes apparent when considering Figure 2.2, which demonstrates the spatial encoding.

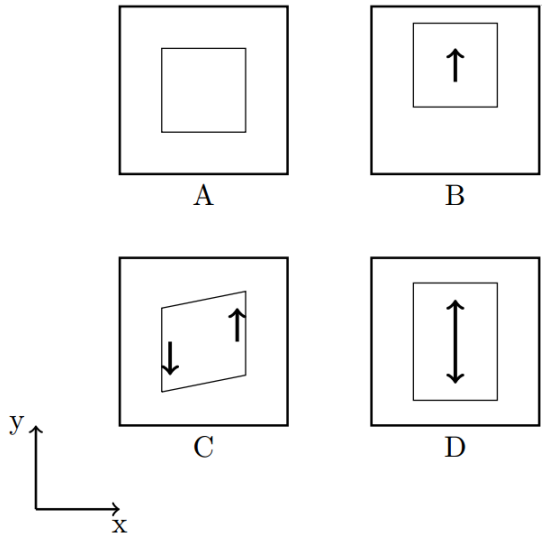

Figure 2.7: *Visualization of geometric distortions introduced by time-independent eddy currents. The x-axis is frequency encoded, and the y-axis is phase encoded. (A) shows the undistorted object, (B) object translation, (C) object shearing and (D) object scaling.*

In EPI, the discrepancy between the bandwidths along the frequency- and phase encoded direction results in these changes being more prominent along the latter. The difference in bandwidth, and by extension, the sampling time for the frequency and phase encoded directions, is visible in Figure 2.4.

The geometric distortions expected from time independent eddy currents are rigid body bulk motion, shear and scaling. In terms of spatial encoding, as described by equation (2.5), translation is caused by the addition of a spatially invariant field component, i.e.

a resulting increase or decrease of the effective static magnetic field from its original value, B_0. Scaling is the result of a change in the spatially varying gradient term, whose behaviour is outlined in Figure 2.2. An increase in the effective gradient amplitude will result in a contraction of the object, whereas a decrease in the amplitude will result in an elongation. Finally, shearing in the phase encoded direction is a result of a frequency direction dependent field component, i.e. the phase encoded gradient for a certain voxel is dependent on said voxels placement along the frequency encoded axis. [11][12]

2.4 Affine Transformation

To correct for motion and eddy current artifacts, a possible method is an Affine transformation [13]. The problem addressed here is to find the optimal alignment between two images.

The basic principle of Affine registration is the simultaneous correction of both eddy current and movement distortions in the image. Time independent eddy current distortions, as detailed in Section 2.3, consists of translation, scaling and shearing, while movement can affect the image as translation and rotation, e.g. azimuthal around an axis. The distortions caused by eddy currents and movement cannot be corrected for sequentially, since they occur according to the scanners and subjects framework, or system of reference, respectively [14].

The registration process defines four distinct distortions, each for three dimensions, resulting in twelve degrees of freedom. The aim of the correction process is to find the optimal value for these parameters, 'fitting' the image being corrected to a chosen standard image.

For the comparison of these images, a cost function is utilized, which when applied to the images, quantifies how 'well' they are spatially aligned. A more in-depth description is available in the citations previously mentioned in this section.

3 Method

Image acquisition was done using two different Siemens 3-Tesla clinical scanners. The scanner models used were Skyra and Prisma from St. Olav's hospital in Trondheim and Haukeland hospital in Bergen, respectively. They both share a slew rate of 200 T/m/s, but the Prisma scanner is capable of a maximum gradient amplitude of 80 mT/m whereas Skyra peaks at 45 mT/m. An overview of the hardware specifications are presented in Table 3.1.

		Skyra	**Prisma**
Gradient system		XQ	XR
Slewrate	[T/m/s]	200	200
Maximum Grad. Amp.	[10^{-3} T/m]	45	80
System weight	[10^{3} kg]	7.3	13
Bore size	[10^{-2} m]	70	60

Table 3.1: *Comparison between hardware specifications[15][16]*

Imaging volume was chosen to cover Corpus Callosum, oriented according to the anterior- and posterior commissure line, or AC-PC line. This can be seen in Figure 3.1b, while Figure 3.1c gives the region of interest (ROI).

Data was acquired using a SEDW imaging sequence, with an echo planar RO. For each scanner, data was acquired with monopolar and bipolar DW gradients.

The b values used for the data acquisition were 0, 350, 700, 1050, 1400, 1750, 2100, 2450, 2800, 3150, 3500, 3800, 4100, 4400, 4700, 5000 s/mm^2. Voxeles were isotropic, with a volume of (2.5 mm)^3. Acquisition matrix size was 92×92, with 11 slices and an interslice-distance of 3 mm. A Partial Fourier acceleration of $^6/_8$ was utilized. A total of 20 diffusion directions, evenly distributed across a half-sphere, were measured. The distribution is visualized in Figure 3.2.

Each sequence was modified according to which scanner and diffusion gradient setup was utilized. Variations are shown in Table 3.2.

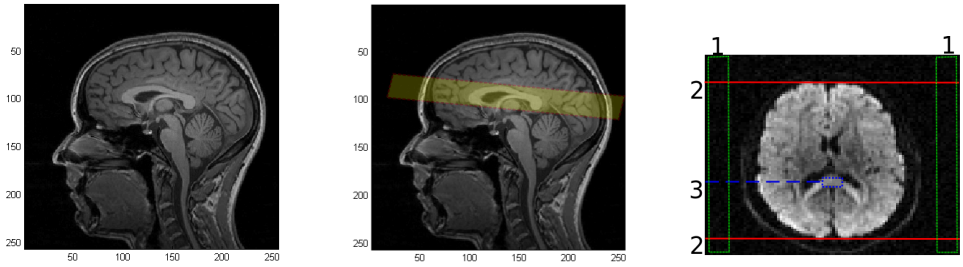

(a) ***(b)*** ***(c)***

Figure 3.1: *(a) Sagittal image slice used to correctly chose an imaging volume, which is displayed in (b), oriented along the AC-PC line. (c) Chosen regions of interest for data analysis. The image, centred in the imaging volume, was acquired with* $b = 1050$ s/mm^2*. (1) Region from which noise was sampled. (2) Solid red lines indicate the image rows used for intensity comparison with regards to geometric distortions, (B) dashed green rectangle indicate ROI for signal averaging and subsequent intensity analysis of diffusion related signal decay.*

	Skyra		Prisma	
	Monopolar	Bipolar	Monopolar	Bipolar
TR	1900	2300	1500	1600
TE	129	124	85	96

Table 3.2: *Sequence parameters*

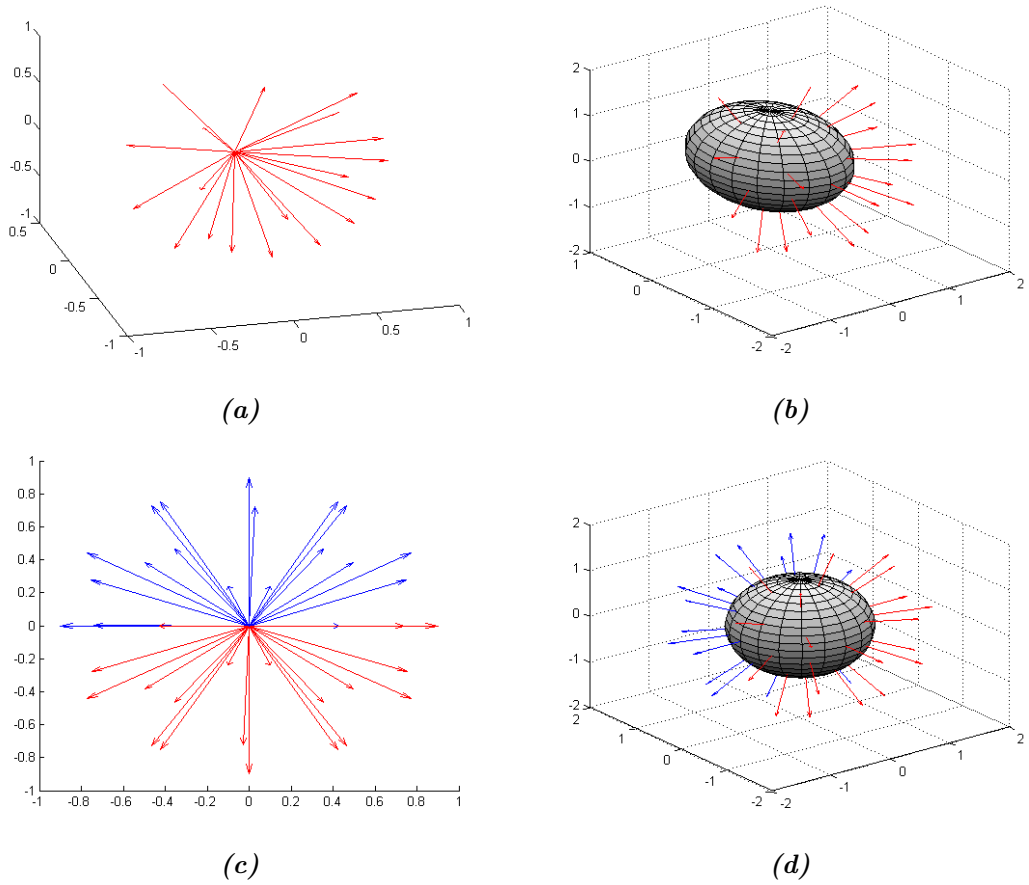

Figure 3.2: *Spatial distribution of diffusion experiment directions. Red arrows indicate the actual experiment directions. Blue arrows merely visualize the total number of directions from which a diffusion constant may be found. Images were created using Matlab R2014a*

3.1 Data Post-Processing

Raw data, and direct image analysis was performed on data in the DICOM-format (Digital Imaging and Communications in Medicine). Images subjected to post-processing, were first imported into NIfTI-format (Neuroimaging Informatics Technology Initiative).

Correction for motion and eddy current distortions was done using MCFLIRT (Motion Correction, FMRIB's (the Oxford centre for Functional MRI of the Brain) Linear Image Registration Tool, from FSL 5.0.8 (FMRIB Software Library)) [17][18][19]. Additionally, the Siemens native correction, Distortion Field Correction (DFC) was also applied to a set of the data for comparison.

4 Result

The initial results were the acquired raw data images. A small sample of these are shown and described briefly in the following section. Subsequent image analysis of SNR and DW metrics is covered thereafter, before the final section deals with the eddy-current artefact analysis.

4.1 Raw Data

The $b = 0$ images are shown in top row of Figure 4.1, along with the $b = 1050$ s/mm^2 images for all experiment directions shown in mosaic format in the bottom row. These were acquired using the sequence setup from Chapter 3, with the parameters from Table 3.2.

Figure 4.2 shows signal evolution for all values of $b > 0$.

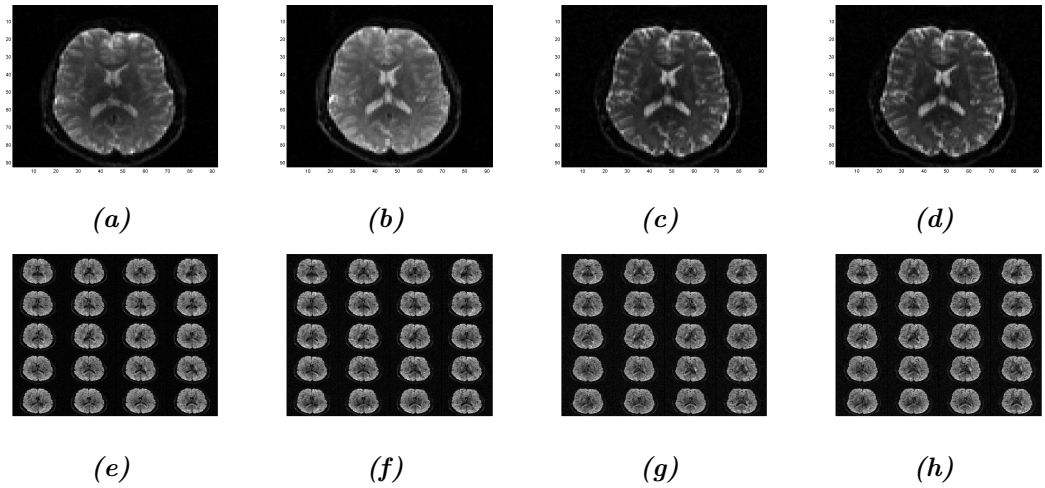

Figure 4.1: *Raw data, image slice from center of the imaging volume. (a)-(d) show the* $b = 0$ *images while (e)-(h) are* $b = 1050$ s/mm^2 *images of all experiment directions shown in mosaic view. (a,e) From monopolar gradient setup from the Prisma scanner (b,f) bipolar, Prisma (c,g) monopolar, Skyra and (d,h) bipolar, Skyra.*

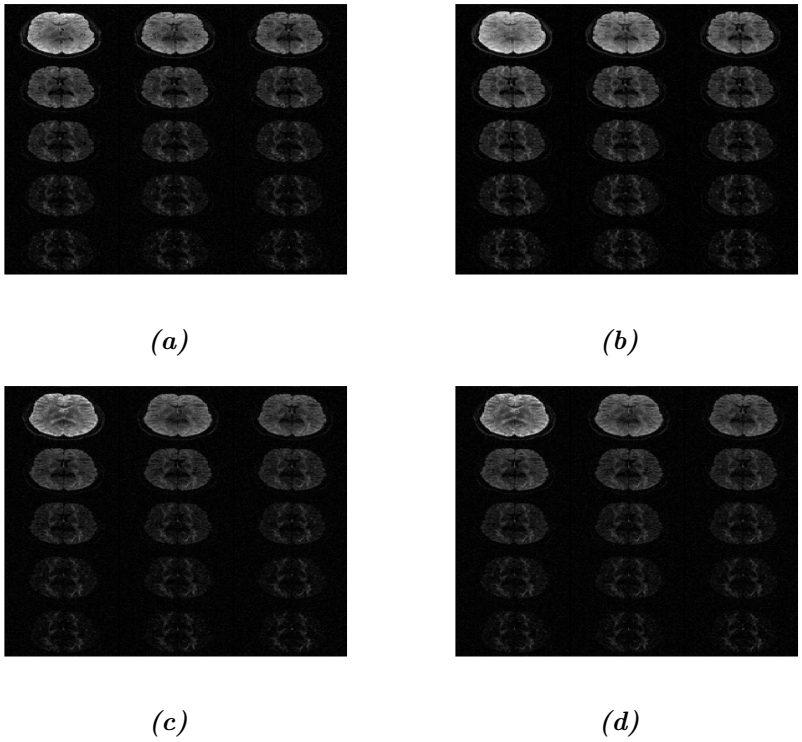

(a) ***(b)*** ***(c)*** ***(d)***

Figure 4.2: *Raw images, showing, in mosaic, signal evolution for all values of b. (a) From monopolar scan from Prisma scanner (b) bipolar, Prisma (c) monopolar, Skyra and (d) Bipolar, Skyra.*

4.2 Measurements

Figures 4.3 and 4.4 showcase the fitting procedure outlined in Chapter 3, which was used during data analysis, with Table 4.1 containing some of the calculated parameters. Reference values for the diffusion in the Splenium were found in [20] to be $\approx 0.7 \times 10^{-3}$ mm^2/s. As shown, the fitting was done for 3, 10 and 15 b-values in addition to the $b = 0$ image from each series. These are shown in each row of images. The columns display, from left to right, the natural logarithm of the signal and the root mean square error of the fitting procedure. The red coloured graph and bars belong to the linear fit, whereas the blue colour represent the second degree polynomial fit. An observed trend for the linear fit, is an increase in error when more data points are included.

The diffusion constants for the different sequences and scanners are shown in Table 4.1.

Table 4.1: *Calculated diffusion constants for the different sequences and scanners. $D_{i,j}$ is the diffusion constant found a curve fit of degree i with j data points used.*

	Skyra		Prisma	
	Monopolar	Bipolar	Monopolar	Bipolar
$D_{1,4}[10^{-3}mm^2/s]$	1.113	0.907	0.914	0.977
$D_{1,11}[10^{-3}mm^2/s]$	0.462	0.426	0.445	0.442
$D_{1,16}[10^{-3}mm^2/s]$	0.288	0.272	0.304	0.298
$D_{2,4}[10^{-3}mm^2/s]$	2.429	1.574	1.755	2.013
$D_{2,11}[10^{-3}mm^2/s]$	1.114	0.962	0.957	0.998
$D_{2,16}[10^{-3}mm^2/s]$	0.778	0.708	0.705	0.706
$C_{2,4}$ $[(10^{-3}mm^2/s)^2]$	1.253	0.635	0.801	0.988
$C_{2,11}[(10^{-3}mm^2/s)^2]$	0.207	0.170	0.162	0.176
$C_{2,16}[(10^{-3}mm^2/s)^2]$	0.097	0.086	0.080	0.081

Signal and noise samples were collected from the regions indicated in Figure 3.1c. Signal graphs for all scanner and gradient combinations are shown in Figure 4.5.

Figures 4.5a and 4.5b show the measured signal for all b-values, with errorbars according to measured background noise. The graphs behave as expected from theory, with an initial steep decay in signal intensity for each increment of b that eventually levels off. A point of interest, however, is the difference in signal between gradient setups on each machine, which is noticeably larger on the Prisma scanner. Figure 4.5c show the registered SNR with Table 4.3 and 4.4 showing a representative selection of the values for the SNR and background noise, respectively.

The background noise is expected to be unaffected by the diffusion sensitizing gradients, which suggests that the graphs should appear similar to the signal graphs. This is the case for both scans performed on the Prisma scanner, and does also appear to be the case

for the DW acquisitions on the Skyra scanner. The Skyra images acquired without DW had an increased level of background noise compared, but neither of the Skyra graphs agree with this prediction. As can be seen in Table 4.4, an increase in background noise is recorded for both gradient setups, resulting in the deviation from expected graph shape.

Table 4.2: *Calculated distribution metrics from the distributions shown in Figures 4.6 according to equations from Section 2.2.1*

	Skyra	
	Monopolar	Bipolar
Mode_{DW} [95%]	6.260 (6.248, 6.271)	6.278 (6.266, 6.290)
$\text{Mode}_{b=0}$ [95%]	10.74 (10.67, 10.82)	10.80 (10.72, 10.88)
Mean_{DW}	7.845	7.868
$\text{Mean}_{b=0}$	13.46	13.537
$\text{Variance}_{\text{DW}}$	16.82	16.91
$\text{Variance}_{b=0}$	49.53	50.07
	Prisma	
	Monopolar	Bipolar
Mode_{DW} [95%]	5.908 (5.902, 5.913)	5.902 (5.894, 5.909)
$\text{Mode}_{b=0}$ [95%]	5.91 (5.89, 5.93)	5.91 (5.88, 5.94)
Mean_{DW}	7.404	7.397
$\text{Mean}_{b=0}$	7.407	7.404
$\text{Variance}_{\text{DW}}$	14.98	14.95
$\text{Variance}_{b=0}$	14.99	14.98

Table 4.3: *Measured SNR from selected ROI, which here was a transverse slice of the Posterior portion of Corpus Callosum, i.e. Splenium.*

	Skyra		Prisma	
	Monopolar	Bipolar	Monopolar	Bipolar
$\text{SNR}(b_0)$	13.95	14.94	37.91	25.14
$\text{SNR}(b_{350})$	20.13	19.39	32.38	21.25
$\text{SNR}(b_{1050})$	17.761	16.20	25.97	18.88
$\text{SNR}(b_{3500}$	14.21	12.84	17.62	13.49
$\text{SNR}(b_{5000})$	13.03	12.27	15.03	11.88

Table 4.4: *Measured average noise for a selection of b-values. The ROI was selected outside the object, in such a location as to avoid traces of ghosting.*

	Skyra		Prisma	
	Monopolar	Bipolar	Monopolar	Bipolar
$\overline{\text{Noise}}(b_0)$	13.4	12.6	6.48	6.10
$\overline{\text{Noise}}(b_{350})$	7.16	7.28	6.77	6.17
$\overline{\text{Noise}}(b_{1050})$	7.50	6.85	6.40	6.20
$\overline{\text{Noise}}(b_{3500}$	7.15	6.93	6.36	6.77
$\overline{\text{Noise}}(b_{5000})$	6.95	7.57	6.04	7.31

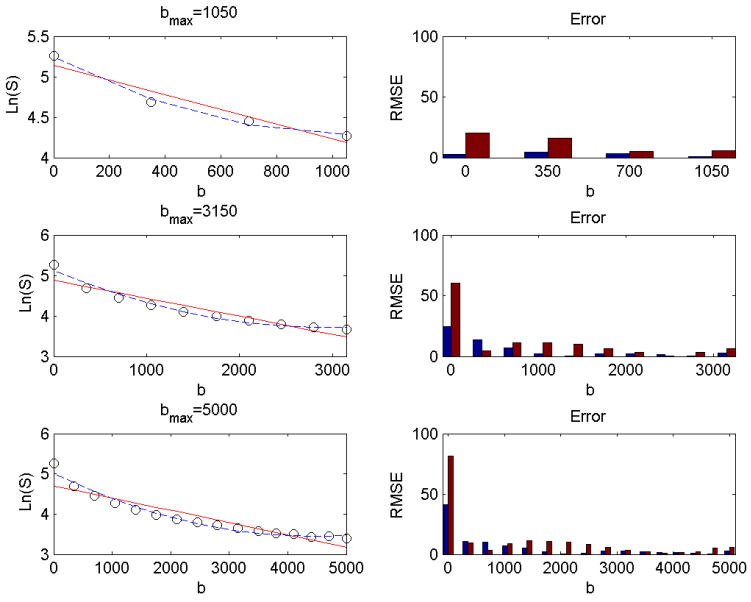

(a) Prisma, Mono

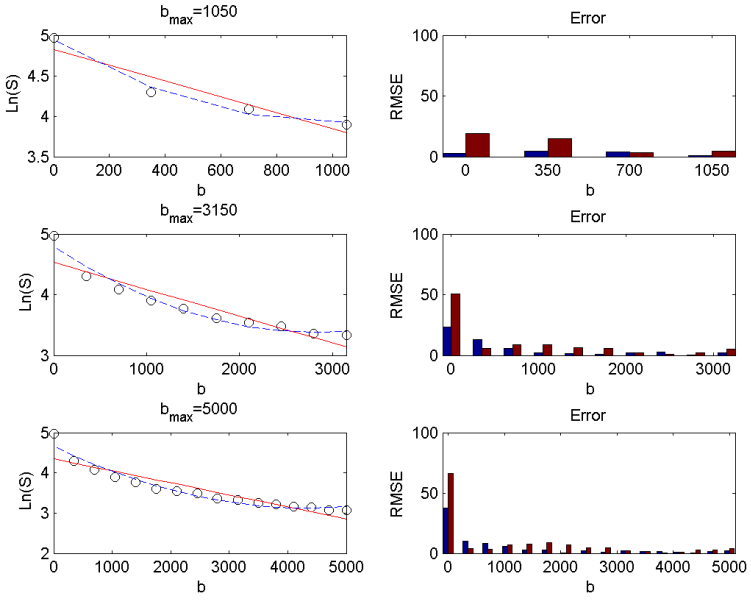

(b) Prisma, Bipol

Figure 4.3: *Curve fitting for measured DW attenuated signal Prisma acquisitions*

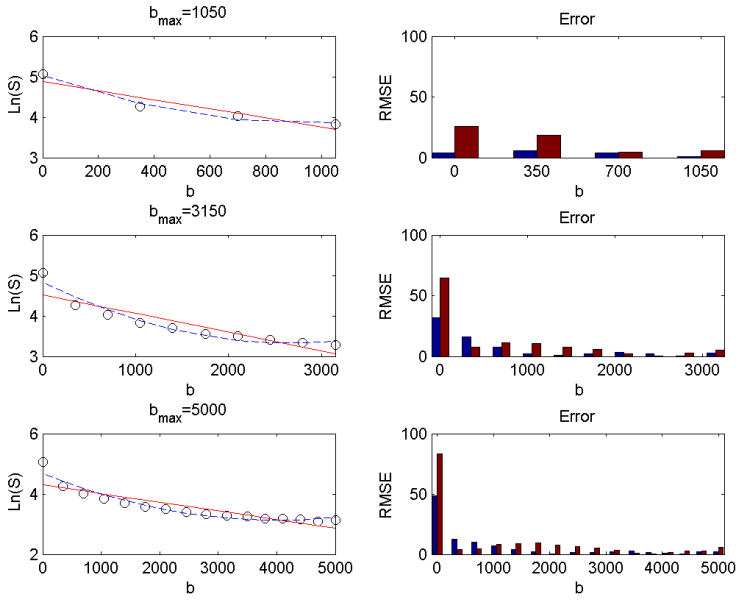

(a) Skyra, Mono

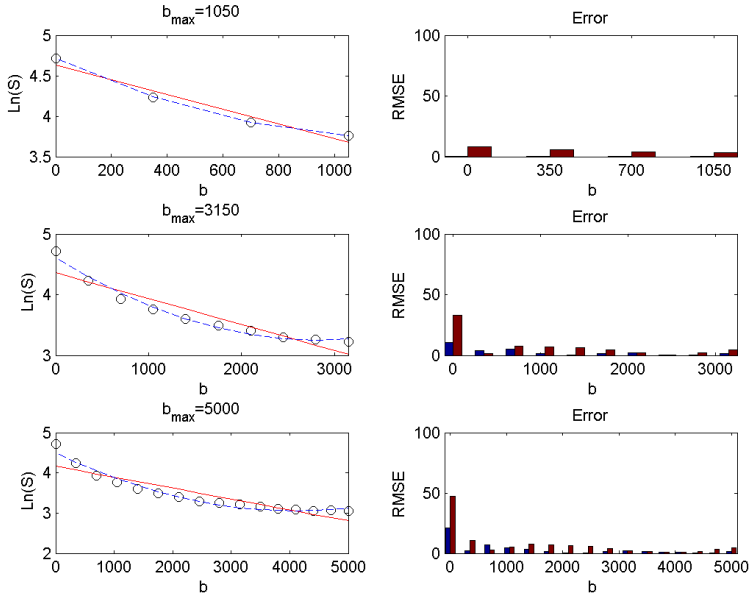

(b) Skyra, Bipol

Figure 4.4: *Curve fitting for measured DW attenuated signal for the Skyra acquisitions.*

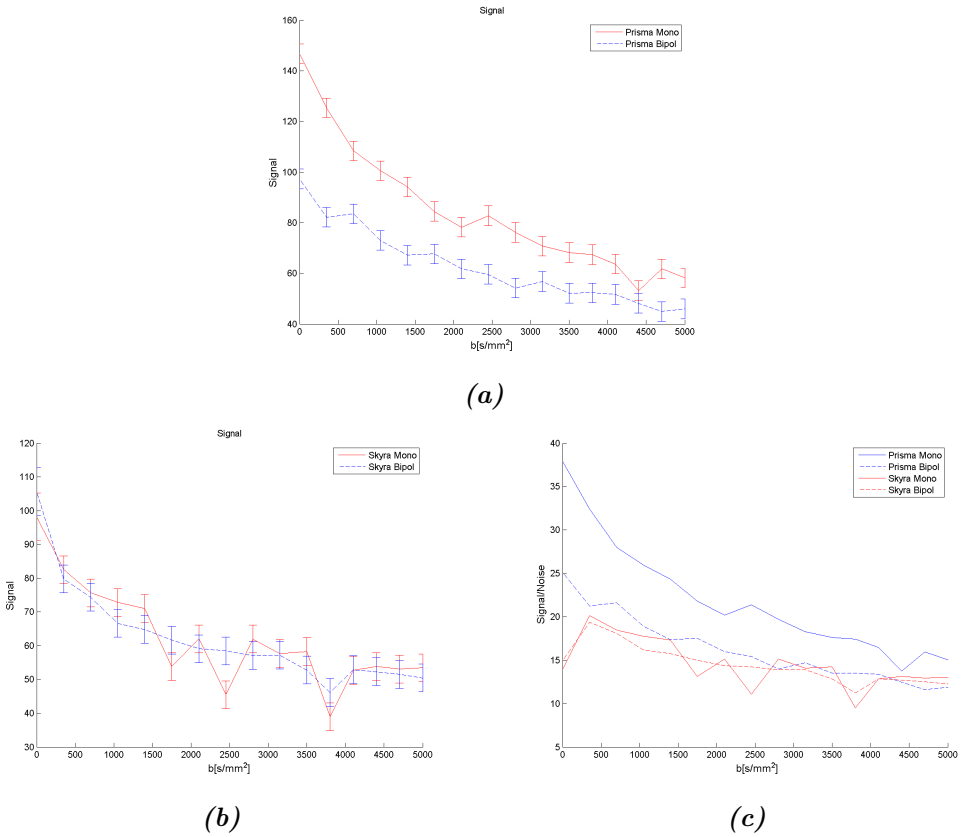

Figure 4.5: *Signal graphs for all scanner and gradient combinations with errorbars showing standard deviation. (c) is all the SNR plotted in the same graph.*

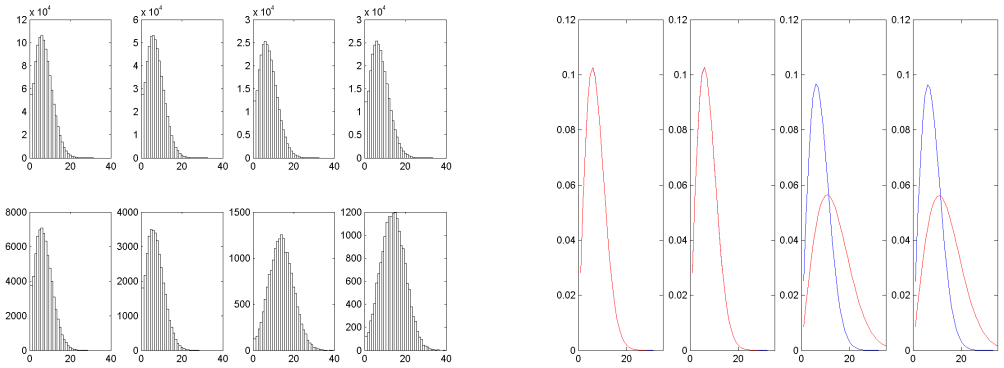

(a) ***(b)***

Figure 4.6: *Noise distribution for all gradient and scanner combinations. From left to right, the columns of each image Prisma: Monopolar, Bipolar and Skyra: Monopolar and Bipolar. (a) show noise sample histograms from DW images (top row) and* b_0 *images (bottom row). (b) Rayleigh probability distribution functions calculated from the histograms, with DW, blue, and* $b = 0$*, red, in each graph.*

4.3 Eddy Current Analysis

Visual inspection of the images revealed small variations in geometry for images along different directions acquired with a certain b-value. This effect was most prominent in the images acquired on the Prisma scanner with the monopolar diffusion gradient setup. A somewhat novel visualization attempt is made in Figure 4.8, which show intensity profiles measured at the anterior and posterior edge of the brain. This profile selection is shown in Chapter 3, Figure 3.1c. An apparent trend in Figure 4.7a is the varying peak intensity for the anterior profiles in the different directions, a variation that is apparently not present to nearly the same extent in Figures 4.7b, and 4.8b

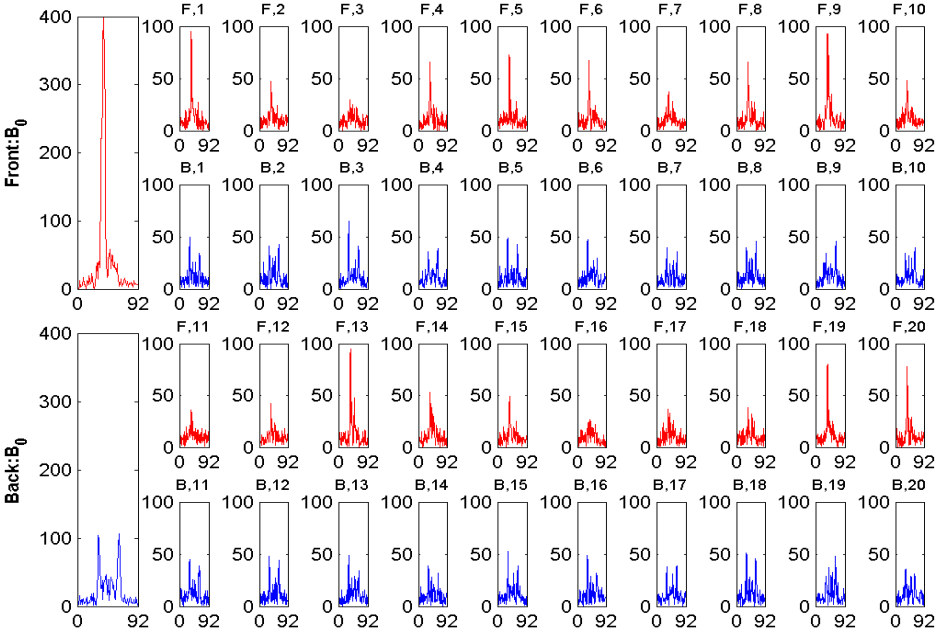

(a) Prisma, Monopolar

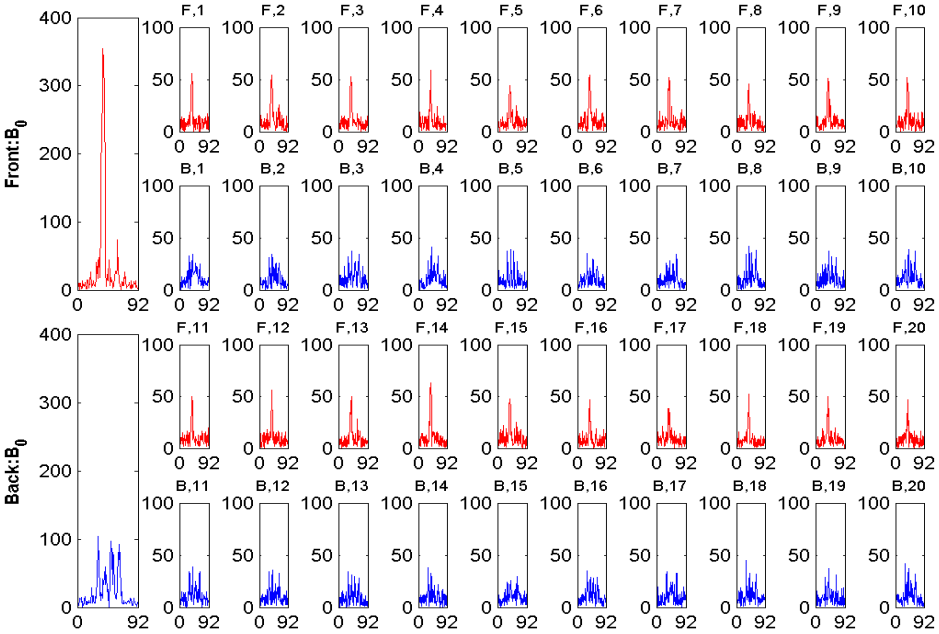

(b) Prisma, Bipolar

Figure 4.7

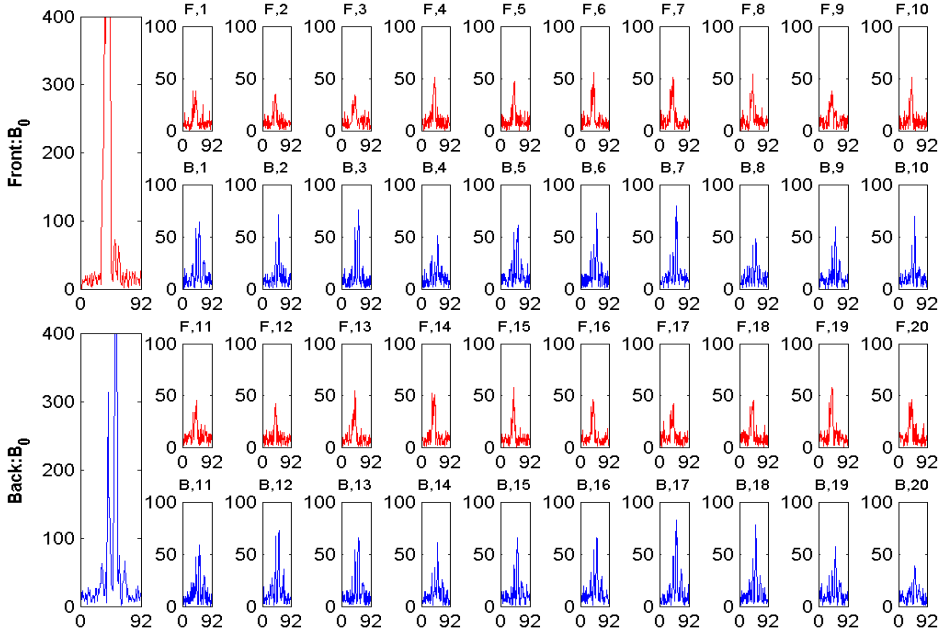

(a) *Skyra, Monopolar*

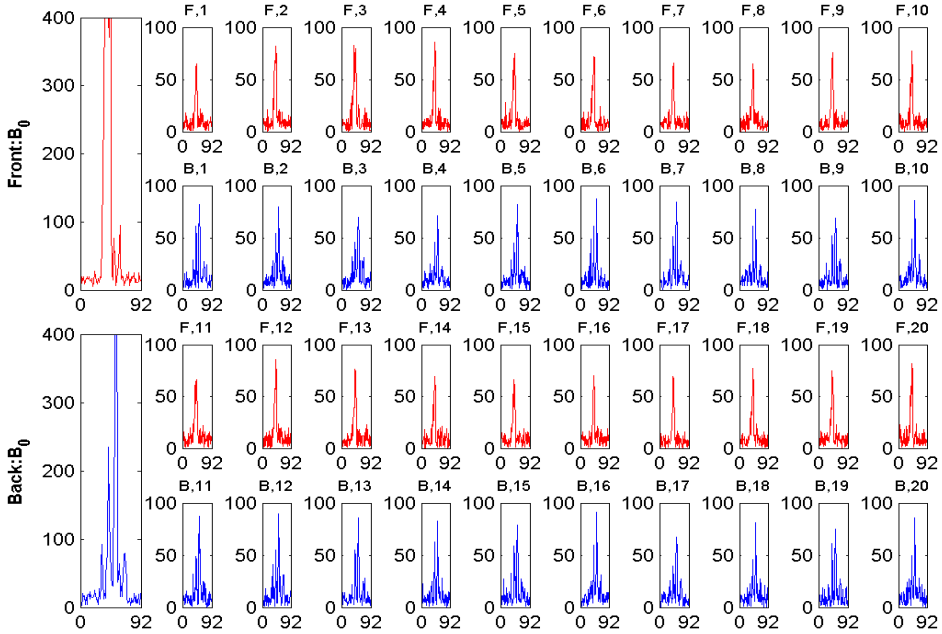

(b) *Skyra, Bipolar*

Figure 4.8: *Image row intensities acquired at the top and bottom edges of the B_0 images for all 20 directions. Larger graphs are B_0, while the smaller images are $b = 1050$. Intensity for anterior and posterior brain edge are coloured red and blue, respectively.*

5 Discussion

The bipolar gradient setup, when performed on the Prisma scanner, suffered a larger drop in signal intensity than was to be expected from the change in TR and TE. As mentioned in section 2.2.5, the increase in TE is expected to reduce the signal intensity according to the transverse relaxation time, T_2. Using equation (2.12), with the sequence parameters from Table 3.2, the theoretically predicted signal values may be calculated. Values of T_1 and T_2 in the Splenium (posterior region of the Corpus Callosum) were determined experimentally by [21] to be ≈ 748 and 75 ms, respectively. For the Prisma scans, the signal attenuation due to longitudinal and transverse relaxation was 0.279 for the monopolar gradient setup, and 0.245 for the bipolar setup, i.e. a ratio of 1.139. The ratio of the measured signals, was 1.501 ± 12.7 %. The same calculation for the Skyra yielded an expected attenuation from longitudinal and transverse relaxation of 0.165 and 0.183 for the monopolar and bipolar setup respectively, with a ratio of 0.902. The measured ratio between the signals were 0.929 ± 26.5 %. This disagreement is visualized in Figure 4.5.

Noise comparison for the Skyra and Prisma datasets revealed that scans acquired on the latter possessed less background noise. This was true overall, but especially for the images acquired without any DW, where the Skyra scanner consistently exhibited a spike in background noise level. This is illustrated in Figure 4.6, where the increase in the mode parameter for the $b = 0$ Skyra scans is apparent. The origin of this anomaly remains unknown, and no precedence was found to have been reported in other research articles. The overall reduction of background noise can stem from a variety of factors. First and foremost is the difference between the Siemens XR and XQ gradient setups. Variations between these, e.g. heating of the gradient coils would introduce thermal noise. Due to the difference in gradient strength, Siemens Prisma most probably possess the superior cooling system of the two scanners to compensate for the increase in max gradient amplitude, but it is difficult to say whether or not it is because of the cooling system that the Prisma exhibit an overall lower background noise level. The systems possess the same slew-rates, but the Prisma can achieve significantly higher gradient values, which could in turn reduce scan time and therefore noise levels. Another detail, is the total weight of the scanner.

The Prisma system is almost twice as heavy, might indicate it is less prone to be affected by physical vibrations. Among the Prisma specifications, there is also a mention of it possessing a "force-compensated design for reduced vibrations". It is again hard to determine whether this merely counteracts the increase in gradient strength, or if it also counteracts other sources of noise that remain present in the Skyra scanner.

The rudimentary fitting procedure performed, visualized in Figures 4.3 and 4.4, show the difference between a linear and second degree polynomial fit for the logarithm of the signal. The root mean square error bar plot is intended purely as a visual aid in discerning how well the curve fits the data points. The linear fit yields the best fit when few points are available, while second degree fitting performs better for higher values of b. This is as predicted by theory, as only the second degree polynomial is able to take deviation from a Gaussian shape into account. Table 4.1 show the calculated values for the diffusion. The diffusion constants calculated under the assumption of unrestricted diffusion, i.e. linear fit, are largest when calculated from few b-values, and reduced when more data points are used. This is to be expected, as the data points acquired with high values of b are expected to exhibit a degree of restricted diffusion.

The second degree polynomial fit also predicts gradually lower diffusion coefficients as more data points are included in the calculation. As opposed to the linear fit, however, the polynomial approaches the expected value of $\approx 0.7 \times 10^{-3}$ mm^2/s as more data points are added. The fitting procedure does not work well with few data points, as can be seen from the overshoot on the diffusion coefficient estimate. This is also reflected in the evolution of C_2 as more data points are added. As a measure of the deviation from a monoexponential decay (a straight line in the logplot), this would be expected to increase as more points are added. The opposite is the case, which might indicate some error in ROI selection or in the calculation procedure. It is also worth noting that all the variables for the second degree polynomial calculated with a total of four data points show large deviations between the different gradient setup and scanner combinations, which indicates that to little data is present to make accurate predictions.

Image slices were compared for a chosen DW along all experiment directions. This revealed slight variations in brain geometry between images. Visual inspection of the data indicated that the geometrical distortions was more prominent in the dataset acquired on the Prisma scanner, using a monopolar gradient setup. This observation is shown in Figure 4.8. It should be stressed, however, that while Figure 4.7a does indeed demonstrate intensity variations for the profiles collected for all directions, it is only in conjunction with the rest of Figure 4.8 that these can be discussed thoroughly. This is due to the intensity variations expected from imaging tissue exhibiting some degree of diffusion anisotropy. Individually, it is therefore difficult to determine whether or not the profile variations are caused by diffusion anisotropy or that the brain has undergone some form of geometry alteration due to patient motion or eddy current artefacts. Profile variations that were caused by diffusion anisotropy would be expected to be

present in all the profile sets, but they appear more prominent in the Prisma scans with monopolar gradients.

Image correction did seemingly improve upon the geometrical distortions, but several of the attempts visually altered the interior of the brain from the original images. The method used in this thesis, FSL's MCFLIRT, also recommends running a brain extraction (i.e. removal of scalp and other non-brain tissue from the image) prior to running their algorithms. This was easily accomplished for lower DW, but the brain extraction program struggled with differentiating between the background noise and the brain for higher DW. To compensate for this, a reference image was provided, as well as testing out several different fractional intensity thresholds. For too small values, non-brain matter and background noise was left on the brain exterior, while higher values resulted in the removal of brain matter as SNR dropped for higher DW.

6 Conclusion

As long as no adequate eddy current correction can be achieved, the Prisma scanner with bipolar gradients appear the superior alternative for data collection. While the drop in signal intensity is greater than expected when compared to the monopolar gradient setup on the Prisma scanner, the removal of first order eddy currents is an absolute requirement preceeding any analysis on a voxel-to-voxel basis. The difference in image quality compared to the Skyra, primarily in the form of slightly reduced levels of background noise, is not particularily large. The difference in background noise for the Skyra systems between DW and $b = 0$ images is however slightly troubling. while this can be compensated for by removing Rician signal bias, as seen in [5] and [4], it is still an anomaly that should warrant further investigation.

6.1 Future Work

If the monopolar diffusion setup is to be utilized, it requires robust eddy current correction. Aside from the method attempted in this project, alternatives such as magnetic field monitoring [22] are potential candidates in the future, but cannot be used to retrospectively correct data that has already been acquired. It would also require additional hardware, to map the magnetic field, which is not standard on most clinical scanners. Another possibility for correction the eddy current distortions, is another FSL algorithm named EDDY. This would, however, require several changes in the sequence parameters. While no explicit lower boundary for number of diffusion directions have been defined, a recommended minimum of ≈ 60 is recommended. The distribution of the directions would also be required to be for a full sphere, rather than the half sphere employed in this thesis. The reason for this is related to the induced eddy currents not necessarily being the exact opposite for opposite directions.

Bibliography

[1] Kristoffersen A. Optimized quantification of diffusional non-gaussianity in the human brain. J Magn Reson Im. 2013;38(6):1434–1444.

[2] Haacke Mea. Magnetic resonance imaging: physical principles and sequence design. Wiley-Liss, New York; 1999.

[3] Bloch F. Nuclear induction. Phys Rev. 1946;70(7-8):460–474.

[4] Sijbers J, Den Dekker A, Poot D, Bos R, Verhoye M, Van Camp N, et al. Robust estimation of the noise variance from background MR data. In: Medical Imaging. International Society for Optics and Photonics; 2006. p. 61446B–61446B.

[5] Gudbjartsson H, Patz S. The Rician distribution of noisy MRI data. Magnet Reson Mede. 1995;34(6):910–914.

[6] Hahn EL. Spin echoes. Phys Rev. 1950;80(4):580.

[7] Schmitt F, Turner R, Stehling MK, Bandettini PA. Echo-planar imaging: theory, technique and application. Springer, Erlangen; 1998.

[8] Qayyum A. Diffusion-weighted Imaging in the Abdomen and Pelvis: Concepts and Applications 1. Radiographics. 2009;29(6):1797–1810.

[9] Stejskal E, Tanner J. Spin diffusion measurements: spin echoes in the presence of a time-dependent field gradient. J Chem Phys. 1965;42(1):288–292.

[10] Miao HC, Wu MT, Kao E, Chiu YH, Chou MC, et al. Comparisons of Reproducibility and Mean Values of Diffusion Tensor Imaging-Derived Indices between Unipolar and Bipolar Diffusion Pulse Sequences. Journal of Neuroimaging. 2015;.

[11] Jezzard P, Barnett AS, Pierpaoli C. Characterization of and correction for eddy current artifacts in echo planar diffusion imaging. Magnet Reson Med. 1998;39(5):801–812.

[12] Ahn C, Cho Z. Analysis of the eddy-current induced artifacts and the temporal compensation in nuclear magnetic resonance imaging. IEEE Trans Med Imag. 1991;10(1):47–52.

[13] Jenkinson M, Bannister P, Brady M, Smith S. Improved optimization for the robust and accurate linear registration and motion correction of brain images. Neuroimage. 2002;17(2):825–841.

[14] Andersson JL, Skare S. A model-based method for retrospective correction of geometric distortions in diffusion-weighted EPI. Neuroimage. 2002;16(1):177–199.

[15] MAGNETOM Prisma; 2015. Available from: `http://www.healthcare.siemens.com/magnetic-resonance-imaging/3t-mri-scanner/magnetom-prisma/technical-details`.

[16] MAGNETOM Skyra; 2015. Available from: `http://www.healthcare.siemens.com/magnetic-resonance-imaging/3t-mri-scanner/magnetom-skyra/technical-details`.

[17] Jenkinson M, Beckmann CF, Behrens TE, Woolrich MW, Smith SM. Fsl. Neuroimage. 2012;62(2):782–790.

[18] Woolrich MW, Jbabdi S, Patenaude B, Chappell M, Makni S, Behrens T, et al. Bayesian analysis of neuroimaging data in FSL. Neuroimage. 2009;45(1):S173–S186.

[19] Smith SM, Jenkinson M, Woolrich MW, Beckmann CF, Behrens TE, Johansen-Berg H, et al. Advances in functional and structural MR image analysis and implementation as FSL. Neuroimage. 2004;23:S208–S219.

[20] Moen KG, Håberg AK, Skandsen T, Finnanger TG, Vik A. A longitudinal magnetic resonance imaging study of the apparent diffusion coefficient values in corpus callosum during the first year after traumatic brain injury. Journal of neurotrauma. 2014;31(1):56–63.

[21] Lu H, Nagae-Poetscher LM, Golay X, Lin D, Pomper M, van Zijl P. Routine clinical brain MRI sequences for use at 3.0 Tesla. J Magn Reson Im. 2005;22(1):13–22.

[22] Chan RW, von Deuster C, Giese D, Stoeck CT, Harmer J, Aitken AP, et al. Characterization and correction of eddy-current artifacts in unipolar and bipolar diffusion sequences using magnetic field monitoring. Journal of Magnetic Resonance. 2014;244:74–84.

A | Sequence parameters

SIEMENS MAGNETOM Skyra syngo MR D13

\\USER\palgo\Head\Jens_PadeDTI\localizer
TA:0:13 PAT:Off Voxel size:0.7×0.7×7.0 mm Rel. SNR:1.00 :fl

Properties

Prio Recon	On
Load to viewer	On
Inline movie	Off
Auto store images	On
Load to stamp segments	On
Load images to graphic segments	On
Auto open inline display	Off
Wait for user to start	Off
Start measurements	single

Routine

Nr. of slice groups	3
Slices	3
Dist. factor	20 %
Position	Isocenter
Orientation	Sagittal
Phase enc. dir.	A >> P
AutoAlign	---
Phase oversampling	0 %
FoV read	250 mm
FoV phase	100.0 %
Slice thickness	7.0 mm
TR	8.6 ms
TE	4.00 ms
Averages	1
Concatenations	9
Filter	Distortion Corr.(2D), Prescan Normalize, Elliptical filter
Coil elements	HEA;HEP

Contrast

TD	0 ms
MTC	Off
Magn. preparation	None
Flip angle	20 deg
Fat suppr.	None
Water suppr.	None
SWI	Off
Averaging mode	Short term
Measurements	1
Reconstruction	Magnitude
Multiple series	Each measurement

Resolution

Base resolution	192
Phase resolution	80 %
Phase partial Fourier	Off
Interpolation	On
PAT mode	None
Image Filter	Off
Distortion Corr.	On
TD	0 ms
Mode	2D
Unfiltered images	Off
Unfiltered images	Off
Prescan Normalize	On
Normalize	Off
B1 filter	Off
Raw filter	Off
Elliptical filter	On
Mode	Inplane

Geometry

Nr. of slice groups	3
Slices	3
Dist. factor	20 %
Position	Isocenter
Phase enc. dir.	A >> P
Phase oversampling	0 %
Multi-slice mode	Sequential
Series	Interleaved
Saturation mode	Standard
Nr. of sat. regions	0
Position mode	L-P-H
Fat suppr.	None
Water suppr.	None
Special sat.	None
Special sat.	None
Table position	P

System

Body	Off
HEP	On
HEA	On
SP5	Off
SP6	Off
SP7	Off
SP8	Off
SP1	Off
SP2	Off
SP3	Off
SP4	Off
Position mode	L-P-H
Positioning mode	ISO
Table position	H
Table position	0 mm
MSMA	S - C - T
Sagittal	R >> L
Coronal	A >> P
Transversal	F >> H
Save uncombined	Off
Coil Combine Mode	Adaptive Combine
AutoAlign	---
Coil Select Mode	Default
Shim mode	Tune up
Adjust with body coil	Off
Confirm freq. adjustment	Off
Assume Dominant Fat	Off
Assume Silicone	Off
Adjustment Tolerance	Auto
? Ref. amplitude 1H	0.000 V
Position	Isocenter
Rotation	0.00 deg
R >> L	350 mm
A >> P	263 mm
F >> H	350 mm
Frequency 1H	123.242634 MHz
Correction factor	1
SRFExcit 1H	61.203 V
Gain	High
Table position	0 mm
Img. Scale. Cor.	1.000

Physio	
1st Signal/Mode	None
Segments	1
Tagging	None
Magn. preparation	None
Dark blood	Off
Resp. control	Off

Inline	
Distortion correction	Off

Sequence	
Introduction	On
Dimension	2D
Averaging mode	Short term
Multi-slice mode	Sequential
Asymmetric echo	Allowed
Contrasts	1
Bandwidth	320 Hz/Px
Flow comp.	No
Allowed delay	0 s
RF pulse type	Normal
Gradient mode	Normal
Excitation	Slice-sel.
RF spoiling	On
TX/RX delta frequency	0 Hz
TX Nucleus	None
TX delta frequency	0 Hz
Coil elements	HEA;HEP
Acquisition duration	0 ms
Mode	Off

BOLD

Subtract	Off
Liver registration	Off
StdDev	Off
MIP-Sag	Off
MIP-Cor	Off
MIP-Tra	Off
MIP-Time	Off
Save original images	On
Distortion Corr.	On
Mode	2D
Unfiltered images	Off
Contrasts	1
Save original images	On
Wash - In	Off
Wash - Out	Off
TTP	Off
PEI	Off
MIP - time	Off

SIEMENS MAGNETOM Skyra syngo MR D13

\\USER\palgo\Head\Jens_PadeDTI\t1_mpr_ns_sag_p2_iso 1mm_iso
TA:4:48 PAT:2 Voxel size:1.0×1.0×1.0 mm Rel. SNR:1.00 :tfl

Properties

Prio Recon	Off
Load to viewer	On
Inline movie	Off
Auto store images	On
Load to stamp segments	Off
Load images to graphic segments	Off
Auto open inline display	Off
Wait for user to start	Off
Start measurements	single

Routine

Nr. of slab groups	1
Slabs	1
Dist. factor	50 %
Position	L4.5 P6.8 F0.2 mm
Orientation	Sagittal
Phase enc. dir.	A >> P
AutoAlign	---
Phase oversampling	0 %
Slice oversampling	0.0 %
FoV read	256 mm
FoV phase	100.0 %
Slice thickness	1.00 mm
TR	2000.0 ms
TE	2.96 ms
Averages	1
Concatenations	1
Filter	Distortion Corr.(2D), Prescan Normalize
Coil elements	HEA;HEP

Contrast

Magn. preparation	Non-sel. IR
TI	1100 ms
Flip angle	8 deg
Fat suppr.	None
Water suppr.	None
Averaging mode	Long term
Measurements	1
Reconstruction	Magnitude
Multiple series	Each measurement

Resolution

Base resolution	256
Phase resolution	100 %
Phase partial Fourier	Off
Interpolation	Off
PAT mode	GRAPPA
Accel. factor PE	2
Ref. lines PE	32
Reference scan mode	Integrated
Image Filter	Off
Distortion Corr.	On
Accel. factor 3D	1
Mode	2D
Unfiltered images	Off
Unfiltered images	Off
Prescan Normalize	On
Normalize	Off
B1 filter	Off
Raw filter	Off
Elliptical filter	Off
Slice resolution	100 %
Slice partial Fourier	Off

Geometry

Nr. of slab groups	1
Slabs	1
Dist. factor	50 %
Position	L4.5 P6.8 F20.2 mm
Phase enc. dir.	A >> P
Phase oversampling	0 %
Slice oversampling	0.0 %
Slices per slab	192
Multi-slice mode	Single shot
Series	Ascending
Nr. of sat. regions	0
Position mode	L-P-H
Fat suppr.	None
Water suppr.	None
Special sat.	None
Table position	P

System

Body	Off
HEP	On
HEA	On
Position mode	L-P-H
Positioning mode	ISO
Table position	F
Table position	0 mm
MSMA	S - C - T
Sagittal	R >> L
Coronal	A >> P
Transversal	F >> H
Save uncombined	Off
Coil Combine Mode	Adaptive Combine
AutoAlign	---
Coil Select Mode	On - AutoCoilSelect
Shim mode	Standard
Adjust with body coil	On
Confirm freq. adjustment	Off
Assume Dominant Fat	Off
Assume Silicone	Off
Adjustment Tolerance	Auto
? Ref. amplitude 1H	0.000 V
Position	L4.5 P6.8 F20.2 mm
Rotation	0.00 deg
F >> H	256 mm
A >> P	256 mm
R >> L	192 mm
Frequency 1H	123.242634 MHz
Correction factor	1
SLoopIRns1 1H	578.285 V
Gain	Low
Table position	20 mm
Img. Scale. Cor.	1.000

Physio

1st Signal/Mode	None
Magn. preparation	Non-sel. IR
TI	1100 ms
Dark blood	Off
Resp. control	Off

Inline

Distortion correction	Off

Sequence

Introduction	On
Dimension	3D
Elliptical scanning	Off
Averaging mode	Long term
Multi-slice mode	Single shot
Reordering	Linear
Asymmetric echo	Allowed
Bandwidth	130 Hz/Px
Flow comp.	No
Echo spacing	8.7 ms
Turbo factor	192
RF pulse type	Normal
Gradient mode	Fast
Excitation	Non-sel.
RF spoiling	On
TX/RX delta frequency	0 Hz
TX Nucleus	None
TX delta frequency	0 Hz
Coil elements	HEA;HEP
Acquisition duration	0 ms
Mode	Off

BOLD

Subtract	Off
StdDev	Off
MIP-Sag	Off
MIP-Cor	Off
MIP-Tra	Off
MIP-Time	Off
Save original images	On
Distortion Corr.	On
Mode	2D
Unfiltered images	Off
Save original images	On

SIEMENS MAGNETOM Skyra syngo MR D13

\\USER\palgo\Head\Jens_PadeDTI\ep2d_diff_pade_tensor
TA:42:14 PAT:Off Voxel size:2.5×2.5×2.5 mm Rel. SNR:1.00 :epse

Properties

Prio Recon	Off
Load to viewer	On
Inline movie	Off
Auto store images	On
Load to stamp segments	Off
Load images to graphic segments	Off
Auto open inline display	Off
Wait for user to start	Off
Start measurements	single

Routine

Nr. of slice groups	1
Slices	10
Dist. factor	20 %
Position	R0.4 P1.3 H0.3 mm
Orientation	T > C-17.7 > S-4.0
Phase enc. dir.	A >> P
AutoAlign	---
Phase oversampling	0 %
FoV read	230 mm
FoV phase	100.0 %
Slice thickness	2.5 mm
TR	2100 ms
TE	124.0 ms
Concatenations	1
Filter	Raw filter
Coil elements	HE1-4

Contrast

MTC	Off
Magn. preparation	None
Fat suppr.	Fat sat.
Fat sat. mode	Strong
Averaging mode	Long term
Measurements	1
Delay in TR	0 ms
Reconstruction	Magnitude
Multiple series	Off

Resolution

Base resolution	92
Phase resolution	100 %
Phase partial Fourier	6/8
Interpolation	Off
PAT mode	None
Distortion Corr.	Off
Prescan Normalize	Off
Normalize	Off
Raw filter	On
Intensity	Weak
Slope	25
Elliptical filter	Off
Dynamic Field Corr.	Off

Geometry

Nr. of slice groups	1
Slices	10
Dist. factor	20 %
Position	R0.4 P1.3 H7.3 mm
Phase enc. dir.	A >> P
Phase oversampling	0 %
Multi-slice mode	Interleaved
Series	Interleaved
Nr. of sat. regions	0
Position mode	L-P-H
Fat suppr.	Fat sat.
Special sat.	None
Fat sat. mode	Strong
Special sat.	None
Table position	P

System

Body	Off
HE1	On
HE3	On
NE1	Off
HE2	On
HE4	On
NE2	Off
SP5	Off
SP6	Off
SP7	Off
SP8	Off
SP1	Off
SP2	Off
SP3	Off
SP4	Off
Position mode	L-P-H
Positioning mode	ISO
Table position	H
Table position	0 mm
MSMA	S - C - T
Sagittal	R >> L
Coronal	A >> P
Transversal	F >> H
Coil Combine Mode	Adaptive Combine
AutoAlign	---
Coil Select Mode	Default
Shim mode	Standard
Adjust with body coil	Off
Confirm freq. adjustment	Off
Assume Dominant Fat	Off
Assume Silicone	Off
Adjustment Tolerance	Auto
? Ref. amplitude 1H	0.000 V
Position	R0.4 P1.3 H7.3 mm
Rotation	0.00 deg
R >> L	230 mm
A >> P	230 mm
F >> H	30 mm
Frequency 1H	123.242634 MHz
Correction factor	1
AddCSaCSatNS 1H	95.153 V
Gain	High
Table position	7 mm
Img. Scale. Cor.	1.000

Physio

1st Signal/Mode	None
Magn. preparation	None
Resp. control	Off

Inline

Distortion correction	Off

Sequence

Introduction	On
Averaging mode	Long term
Multi-slice mode	Interleaved
Bandwidth	2012 Hz/Px
Optimization	None
Free echo spacing	Off
Echo spacing	0.56 ms
EPI factor	92
RF pulse type	Normal
Gradient mode	Fast*
TX/RX delta frequency	0 Hz
TX Nucleus	None
TX delta frequency	0 Hz
Coil elements	HE1-4
Acquisition duration	0 ms

BOLD

Delay in TR	0 ms
Diffusion mode	MDDW
Diff. weightings	16
b-value 1	0 s/mm²
Diff. weighted images	On
Trace weighted images	On
ADC maps	On
FA maps	On
Mosaic	On
Tensor	On
Distortion Corr.	Off
b-Value >=	0 s/mm²
Exponential ADC Maps	Off
Invert Gray Scale	Off
Calculated Image	Off